ACS APPLIED MATERIALS & INTERFACES

Research Article

www.acsami.org

Buried Charge at the $TiO_2/SrTiO_3$ (111) Interface and Its Effect on Photochemical Reactivity

Yisi Zhu, Paul A. Salvador, and Gregory S. Rohrer*

Carnegie Mellon University, Department of Materials Science and Engineering, Pittsburgh, Pennsylvania 15213, United States

Supporting Information

ABSTRACT: High-temperature annealing in air is used to produce $SrTiO_3$ (111) surfaces with two types of atomically flat terraces: those that promote photoanodic reactions and those that promote photocathodic reactions. Surface potential measurements show that the photocathodic terraces have a relatively more positive surface potential than the photoanodic terraces. After depositing thin TiO_2 films on the surface, from 1 to 13 nm thick, the surface of the film above the photocathodic terraces also has photocathodic properties, similar to those of the bare surface. While a more positive surface potential can be detected on the surface of the thinnest TiO_2 films (1 nm thick), it is undetectable for thicker films. The persistence of the localized photocathodic properties on the film surface, even in the absence of a measurable difference in local potential, indicates that the charge associated with specific terraces on the bare $SrTiO_3$ (111) surface remains localized at the $TiO_2/SrTiO_3$ interface and that the buried charge influences the motion of photogenerated carriers.

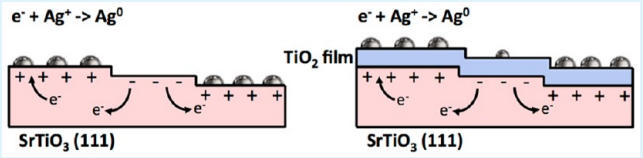

KEYWORDS: *$SrTiO_3$, TiO_2, heterostructure, photochemical reactivity, atomic force microscopy*

1. INTRODUCTION

Studies of polar surfaces such as ZnO (0001)[1] and GaN (0001)[2] have shown that the internal electric field that arises from the charge on the polar surface can separate photogenerated electron−hole pairs and increase their photochemical reactivity. $SrTiO_3$ is a well-known photocatalyst that can split water when illuminated by UV light,[3−5] and several of the low-index surfaces are polar. For example, the ideal unreconstructed (111) surface is polar and charged; it can be terminated by a Ti^{4+} layer or by a $(SrO_3)^{4-}$ layer. While the real $SrTiO_3$ (111) surface in air is likely to be reconstructed[6−8] and covered by a layer of adsorbates,[9,10] it has been shown that some (111) terraces have locally photocathodic properties and the others have photoanodic properties.[11] Furthermore, the photocathodic terraces have a relatively positive potential compared the photoanodic terraces, as measured by Kelvin probe force microscopy (KFM).[12] The interpretation of these observations was that the terraces with a more positive potential (photocathodic) have reduced upward band bending at the surface, and it is easier for photogenerated electrons to reach the surface and participate in photoreduction reactions. The photoanodic terraces, with a less positive surface potential, have increased upward band bending that prevents electrons from getting to the surface while holes are driven to the surface to participate in oxidation reactions. In other words, the polar terraces on the $SrTiO_3$ (111) surface have distinct photocathodic or photoanodic properties and, therefore, strongly influence photochemical reactions.

While polar surfaces might provide a mechanism to increase photochemical reactivity, their stability with respect to faceting and other types of reconstruction is questionable.[13,14] One strategy for stabilizing polar surfaces is to add a thin coating that protects the polar surface.[15−17] This may or may not be necessary for $SrTiO_3$, whose native surfaces are relatively stable in photochemical reactions, especially compared to other complex oxides. However, the stabilities of $SrTiO_3$ surfaces that have been processed to be more photocathodic or photoanodic, as in ref 12, are not yet known. Earlier studies of ferroelectrics coated by TiO_2 have illustrated that the reactivity of the film surface is spatially selective and mimics the reactivity of the underlying polar substrate.[15,17] The proposed mechanism is essentially the same as for the bare ferroelectric surface;[18] the substrate surfaces with positively charged domains have reduced upward band bending, and the substrate surfaces with negatively charged domains have increased upward band bending. Electrons and holes photogenerated in the substrate migrate to positive and negative domains, respectively, and can then pass through the relatively thin TiO_2 coating and react with species at the surface. Recent simulations of photogenerated charge carrier transport in coated ferroelectrics provided quantitative support for this mechanism and suggested that further improvements can be made by the addition of electrocatalytic coatings.[19,20]

Considering the similarities between charged ferroelectric domains and polar surface terminations, we can hypothesize that a thin TiO_2 coating on a polar $SrTiO_3$ surface will have, if the buried charge can be preserved at the interface, photocathodic and photoanodic regions that mimic the reactivity of

Received: December 21, 2016
Accepted: February 13, 2017
Published: February 13, 2017

DOI: 10.1021/acsami.6b16443
ACS Appl. Mater. Interfaces 2017, 9, 7843−7851

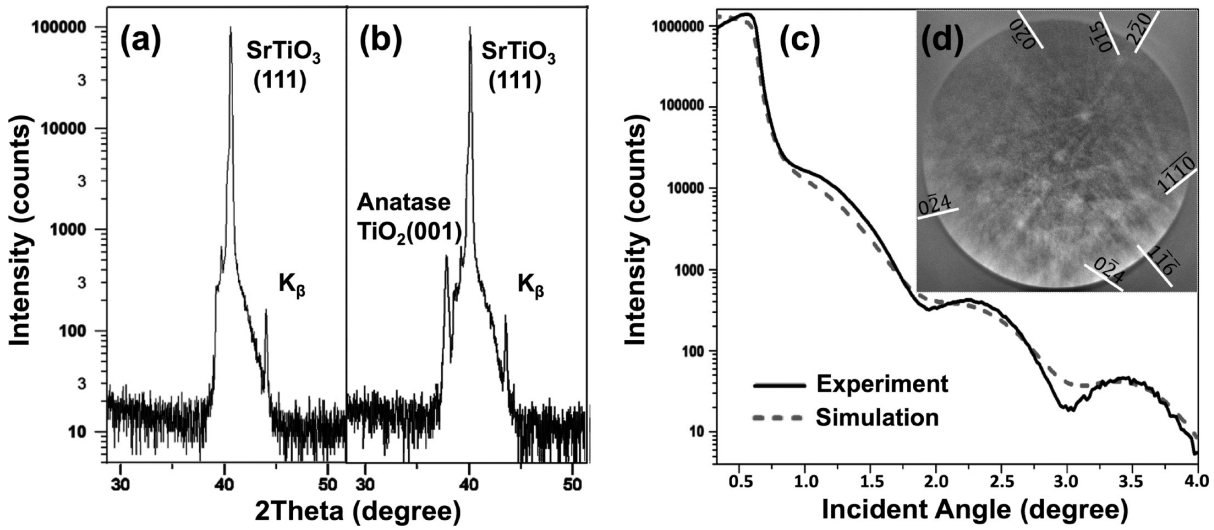

Figure 1. XRD patterns of (a) the bare $SrTiO_3$ (111) substrate and (b) the $TiO_2/SrTiO_3$ heterostructure. Film thickness is about 50 nm. (c) Example of an X-ray reflectivity curve measured on a TiO_2 film/$SrTiO_3$ (111) single-crystal heterostructure. (d) Electron backscatter diffraction pattern from the 50 nm thick TiO_2 film on $SrTiO_3$ (111).

the underlying substrate. The main point of this paper is to describe findings that support this hypothesis. TiO_2 is a reasonable choice for the coating because it has been used to coat ferroelectrics and $SrTiO_3$ in the past,[15,21] it is a stable photocatalyst,[22,23] and the $TiO_2/SrTiO_3$ heterostructure has been shown to be photocatalytically active.[24] $SrTiO_3$ (111) surfaces have been prepared by high-temperature annealing, and the photocathodic regions have been identified using both surface potential imaging by KFM and the photochemical reduction of silver. After growing thin TiO_2 films, the same areas were analyzed and the results show that the charge on the terraces of the bare $SrTiO_3$ surface remains at the buried interface and influence the transport of photogenerated charge carriers.

2. EXPERIMENTAL PROCEDURE

Commercially available $SrTiO_3$ (111) single crystals (MTI Co., Richmond, CA, (111) ± 0.5°, roughness < 5 Å) were heated in air at 5 °C/min to 1250 °C and held for 10 h. After annealing, the topography and surface potential distribution were imaged using a scanning probe microscope (Solver-Next, NT-MDT, Russia). A silicon probe (Tap300-G, BudgetSensors, Bulgaria) was used to record topographic images, and a conductive PtCr-coated probe (190E-G, BudgetSensors, Bulgaria) was used to record surface potential (also referred to as KFM) images. The image data was processed using the Gwyddion[25] software package.

The photocathodic areas of the surface were identified by photochemically reducing Ag^+ from solution.[11,18,26,27] The reduced silver is insoluble and forms metallic deposits on the surface that can be imaged by AFM.[28] In this experiment, a Viton O ring (diameter ~0.5 cm) is placed on the surface, a 0.115 M aqueous solution of $AgNO_3$ was poured into the O ring, and a quartz slip was placed on top, sealing the solution in the O ring by capillarity without an air bubble. The assembly was then illuminated with a 300 W mercury lamp (Newport, Irvine, CA) for 8 s. During this procedure, skin and eyes must be protected to prevent damage from UV radiation. After illumination, the sample was rinsed with deionized water and dried using a stream of 99.995% nitrogen gas. After imaging the pattern of silver on the surface, the silver was removed by wiping the surface with a cotton swab and then sonicating the sample in a bath of methanol for 10 min. After the surface was cleaned, it was imaged by AFM again to make sure there was no detectable silver residue.

TiO_2 thin films were grown on the clean $SrTiO_3$ (111) surface using pulsed laser deposition (PLD) (Neocera, MD) with a KrF (λ = 248 nm) laser (Coherent, CA). The films were deposited at 700 °C with an oxygen pressure of 30–40 mTorr. These conditions were adopted, with minor adjustments, from previous work in which TiO_2 films were grown on $BiFeO_3$ and $BaTiO_3$ substrates.[15,17,29] Note that to make the film as smooth as possible, we used a reduced laser pulse frequency (3 Hz) and a reduced laser energy (estimated to be 0.6 J/cm^2 at the target). After deposition, the film thickness was measured using X-ray reflectivity. Films thicker than 5 nm can be measured directly, and the thicknesses of thinner films were estimated from the number of pulses used during the deposition (calibrated from the measurements on the thicker films). The film growth rate in these conditions is around 1 nm per 1400 pulses. The phase of the film was examined by X-ray diffraction. A Philips X'Pert Pro MRD system was used for the diffraction measurements. The Cu anode X-ray source was operated at 40 kV and 45 mA to generate an X-ray beam with a wavelength of 0.154 nm (Cu $K\alpha_1/K\alpha_2$). Electron backscatter diffraction patterns of the heterostructure were captured using a Quanta 200 SEM (FEI, Hillsboro, OR) and analyzed using commercial software (TSL, EDAX, Mahwah, NJ) to further characterize the crystallinity and orientation of the films.

The film surfaces were used to reduce silver under the same conditions as the bare substrates. Topographic atomic force microscopy (AFM) images were recorded of the same areas before and after depositing the film so that the patterns of silver reduced on the film could be compared to those on the bare substrate. KFM was also used to map the surface potential distribution in the same areas before and after film growth. It was possible to locate and image the same areas at different stages of the experiment by navigating the microscope with reference to visible fiducial marks deliberately added to the sample surface.

3. RESULTS

X-ray diffraction was used to characterize the bare annealed $SrTiO_3$ (111) substrate and the 50 nm $TiO_2/SrTiO_3$ heterostructure. The diffraction patterns from the bare substrate and the heterostructures are shown in Figure 1a and 1b, respectively. When they are compared, it is clear that a new peak has appeared after deposition of the 50 nm film. The position of the $SrTiO_3$ (111) peak is 40.081°, shifted by +0.082° from the ideal peak position (39.999°).[30] The film peak is located at 37.812°. Assuming that the measured position

DOI: 10.1021/acsami.6b16443
ACS Appl. Mater. Interfaces 2017, 9, 7843–7851

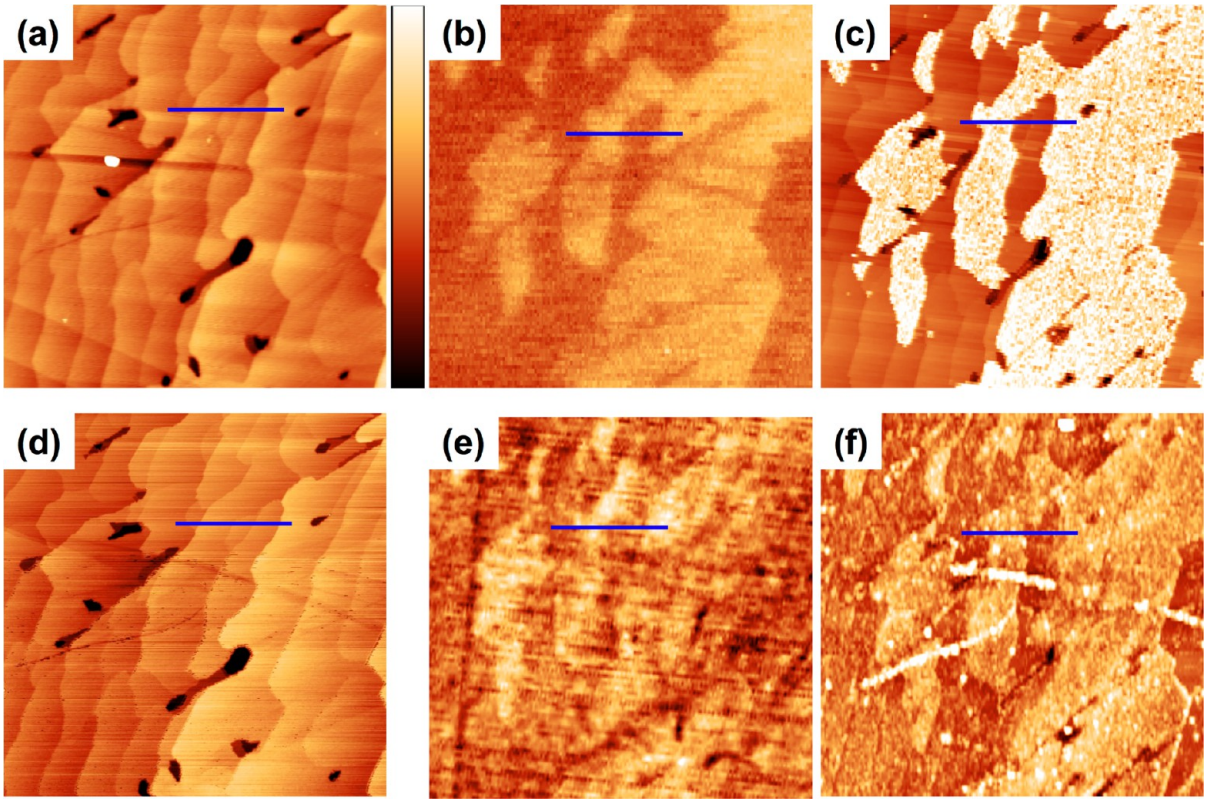

Figure 2. (a and d) Topographic AFM images and (b and e) surface potential images before the reaction, and (c and f) topographic images of the same areas after photochemical reduction of Ag^+. (a–c) Images of a bare $SrTiO_3$ surface and (d–f) a 1 nm thick TiO_2 film surface supported on the same $SrTiO_3$ (111) substrate at the same location. Field of view for all images is 5 μm × 5 μm. Coloring scheme used in all images in this paper is illustrated between panels a and b, where black (white) is assigned to the lowest (highest) numerical value. In these images, the black-to-white contrast range is (a and d) 0–5 nm, (b) 0–30 mV, (e) 0–20 mV, and (c and f) 0–10 nm.

of the new peak is shifted by the same offset as the $SrTiO_3$ (111) peak, its true position is 37.730°. We assign this new peak to anatase (004) because it differs from the ideal position by only 0.028°.[31] It has been reported that TiO_2 films grown on $SrTiO_3$ (111) can have mixed phases and orientations: in addition to (001) anatase, (112) anatase and (100) rutile are also observed.[32] However, the (112) anatase diffraction peak (38.600°) and the rutile (200) peak (39.195°) coincide with the $SrTiO_3$ (111) substrate peak, so the X-ray diffraction data was not sufficient to determine if these other orientations exist.

A typical X-ray reflectivity pattern is shown in Figure 1c. The film thickness is directly proportional to the spacing between local maxima, while the overall intensity is also related to the substrate and film roughness. Using the X'Pert Reflectivity simulation software,[33] the pattern was simulated using a film (substrate) roughness of ~4 Å (0 Å) and a film thickness of 7.5 nm. Note that the maximum incident angle range in the measurement is 4°; beyond 4° the intensity is less than the noise level. Therefore, the thinnest films that the X-ray reflectivity technique can characterize are around 5 nm, which will only show two maxima in the reflection intensity. Using the growth rate data from the thickest films, a series of films with thicknesses from 1 to 25.5 nm were deposited.

An electron backscatter diffraction pattern of a 50 nm thick TiO_2 film is shown in Figure 1d. The diffraction pattern shows some obvious bands but is relatively weak and could not be indexed to a single phase, though some bands (labeled in Figure 1d) were consistent with the anatase (001) orientation. The overall pattern is best described as arising from several orientations or phases, indicating the film is polycrystalline. The above results indicate that the films are flat (supported later by AFM measurements), likely from kinetic factors including low relative adatom mobility. Furthermore, they have crystallites with small lateral spatial extents and several orientations, likely from specifics of the deposition conditions and the substrate surface itself, the former of which were targeted to yield smooth films and the latter of which were chosen to yield surfaces with specific photocatalytic properties. Such films are reasonable for our studies because polycrystalline films are characteristic of what would be expected in a real catalyst. Furthermore, previous studies of TiO_2-coated $BaTiO_3$ showed that the phase and orientation of the TiO_2 had little effect on the reactivity, which was dominated by the substrate polarity.[34] We expect the same to be true here.

The topography of the $SrTiO_3$ (111) surface after annealing at 1250 °C in air is shown in Figure 2a. The surface is characterized by a set of atomically flat terraces separated by approximately parallel steps 1–2 nm in height. The roughness of a single terrace on the $SrTiO_3$ (111) substrate is <0.02 nm, much less than the height between parallel layers, and we therefore refer to the terraces as "atomically flat". The surface potential distribution in the same area is shown in Figure 2b. The surface potential image indicates that the terraces have two distinct contrast levels, and the potential difference between the two varies in the range of 7–15 mV. After the sample was illuminated by UV light in a silver nitrate solution, metallic silver selectively deposited on some of the terraces and appears as white contrast in Figure 2c; the deposits have a height of

DOI: 10.1021/acsami.6b16443
ACS Appl. Mater. Interfaces 2017, 9, 7843–7851

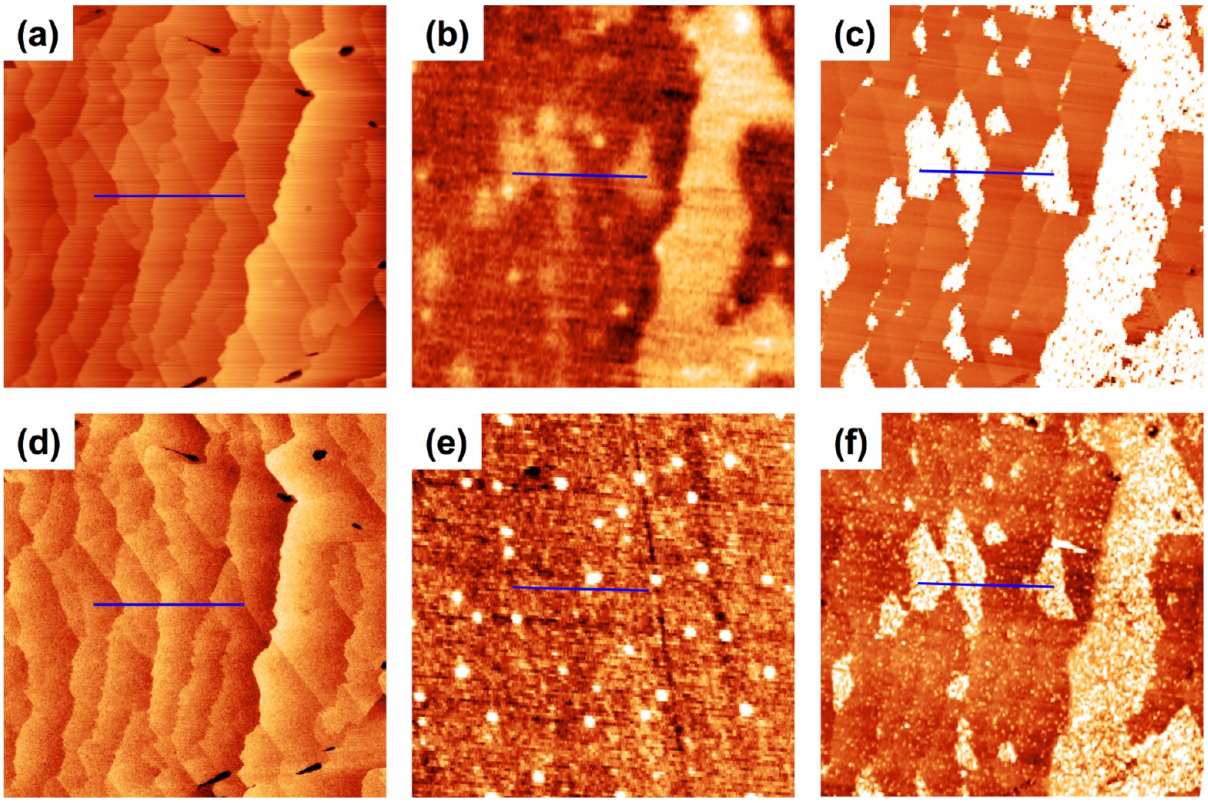

Figure 3. (a and d) Topographic AFM images and (b and e) surface potential images before the reaction, and (c and f) topographic images of the same areas after photochemical reduction of Ag^+. (a–c) Images of the bare $SrTiO_3$ surface and (d–f) a 7.5 nm thick TiO_2 film surface supported on the same $SrTiO_3$ (111) substrate at the same location. Field of view for all images is 5 μm × 5 μm. In these images, the black-to-white contrast range is (a and d) 0–5 nm, (b) 0–25 mV, (e) 0–20 mV, and (c and f) 0–10 nm.

approximately 5 nm. After comparing the locations of the silver to the potential distribution in the KFM image (Figure 2b), it is clear the Ag deposits preferentially on the set of terraces that have the relatively greater (more positive) surface potential. These observations are consistent with those we have recently reported, and we refer to the terraces that reduce silver as photocathodic terraces.[12]

The reduced silver was removed from the surface, and a 1 nm thick TiO_2 film was deposited. A topographic AFM image (Figure 2d) and a KFM image (Figure 2e) were recorded of the film surface at the same location where the images in Figure 2a–c were recorded. There is no obvious topographic change after film deposition, and the roughness on the terrace is approximately 0.04 nm, indicating that the film is also atomically flat on each terrace. The potential contrast measured on the film surface (Figure 2e) is similar to that measured on substrate (Figure 2b), though the measured potential differences between types of terraces for the film (3–8 mV) are less than those for the substrate (7–15 mV). The topography of the same area of the film's surface after photoreduction of silver is shown in Figure 2f. The pattern of silver on the film surface is similar to that observed on the substrate surface before film deposition. In the case of the film, some silver deposits appear everywhere on the film, but significantly more silver is observed on the terraces with a higher potential. In other words, regions above the photocathodic terraces on the bare substrate are also photocathodic on the surface of the covering film. Additional images of this sample with a 15 μm × 15 μm field of view, illustrating the same features in Figure 2, are displayed in Figure S1 (Supporting Information).

The experiment described above was repeated but using a thicker, 7.5 nm TiO_2 film, and the results are illustrated in Figure 3. The images in Figure 3a, 3b, and 3c illustrate the topography of the clean substrate, the surface potential, and the topography after the photochemical reduction of silver, respectively. The images in Figure 3a–c have the same characteristics as those in Figure 2a–c. Specifically, the measured surface potential of the atomically flat terraces is correlated to the location of the photochemcially reduced silver. After removing the silver and depositing a 7.5 nm thick TiO_2 film, images of the same area were recorded before (Figure 3d and 3e) and after (Figure 3f) the photochemical reduction of silver. Comparing Figure 3a and 3d, the film is obviously rougher than the substrate, but the shapes of the step edges and terraces are unchanged. Thus, it is possible to verify that the image is recorded at the same location. The KFM image contrast (Figure 3e) of the film is not similar to that of the substrate (Figure 3e), and it thus differs from the corresponding image of the 1 nm film (Figure 2e). The potential contrast in Figure 3e may be related to the polycrystalline nature of film, as different TiO_2 phases and orientations have different work functions, which contribute to the local surface potential. Even though the potential distribution on the substrate is not visible in the KFM image, the pattern of reduced silver (Figure 3f) still mimics that found on the bare substrate (Figure 3c). This result suggests that the charge on the buried substrate terraces remains and influences the motion of photogenerated carriers but is screened by the film so that it is not detected by the KFM tip which is above the surface.

DOI: 10.1021/acsami.6b16443
ACS Appl. Mater. Interfaces 2017, 9, 7843–7851

Additional images of this sample with a 15 μm × 15 μm field of view, illustrating the same features in Figure 3, are displayed in Figure S3 (Supporting Information). The experiments described above, using 1 and 7.5 nm thick TiO_2 films, were also carried out using samples with 2 and 13 nm thick TiO_2 films; the results from these experiments are shown in Figures S2 and S4, respectively, in the Supporting Information. The results from the 2 and 13 nm thick TiO_2 films are similar to what was observed for the 7.5 nm thick film. Specifically, the potential contrast in the KFM images of the substrate does not appear in KFM images of the film, but the pattern of reduced silver on the film surface is similar to what was observed on the substrate surface before film deposition.

In the crystal structure of $SrTiO_3$, neighboring Ti^{4+} and $(SrO_3)^{4-}$ (111) layers are separated by N = 1.12 Å. Terraces separated by an even-N step height are of the same surface composition, while terraces separated by an odd-N step height have different surface composition. These step height differences have also been demonstrated experimentally and have been shown to correlate with photochemical reactivity and surface potential measurements.[11,12] The height and surface potential profile measured on the bare substrate along the (blue) line drawn on Figure 2a and 2b are plotted in Figure 4a,

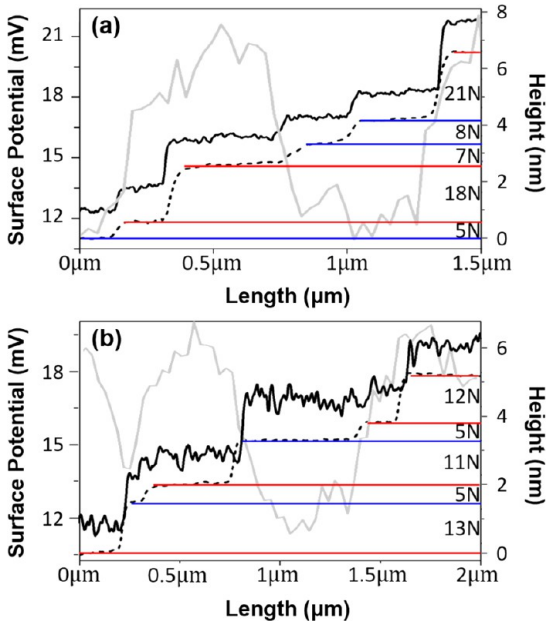

Figure 4. Surface potential and height measurements extracted from images in Figures 2 and 3 at the positions of the blue lines; (a) substrate and 1 nm film and (b) substrate and 7.5 nm film. Black dashed lines and light gray solid lines are the height and surface potential profiles from the bare $SrTiO_3$ substrates, respectively. Black solid lines are the height profiles from the same locations on the film surfaces. Average heights of photocathodic (photoanodic) terraces are marked with red (blue) lines in the image. All step heights are integer multiples of the interplanar spacing N (N = 1.12 Å).

respectively, using a black dashed line and light gray solid line. The average heights of the photocathodic terraces are marked with solid red lines. The other terraces, shown to be photoanodic in previous work,[11,12] are marked with solid blue lines. From left to right, the line traverses six terraces. We define the height of the first terrace as 0 Å, for reference, and determine the heights (number of N layers) of the second to sixth terraces as 5.7 (5N), 25.7 (23N), 33.4 (30N), 42.2 (38N), and 65.7 Å (59N). Note that the N in parentheses corresponds to the difference from the reference at 0 Å, while the N marked in Figure 4 corresponds to the height difference between neighboring terraces. After correlating the step heights with the surface potential profile, we find all photocathodic terraces have higher surface potentials (18−22 mV) and because they are separated by even-N step heights have the same surface composition. The remaining nonphotocathodic terraces have lower surface potentials (11−13.5 mV) and because they are separated by even-N step heights, have the same surface composition.

The height profile extracted from the film surface at exactly the same location is plotted with a solid black line in Figure 4a. There is no significant change for the step heights measured on the film surface, indicating the films are flat and the growth rate did not depend on the composition of the terrace. The surface roughnesses of single terraces, represented by the standard deviation of the height, were also calculated from these data. For the bare $SrTiO_3$ substrate, the roughnesses of single terraces were between 0.1 and 0.2 Å, while the roughnesses of the film terraces were between 0.4 and 0.5 Å; therefore, the 1 nm thick film is considered atomically flat, and the substrate terrace structures appear to have been well preserved at the film surface.

The results from the substrate and 7.5 nm thick film, extracted from the positions of the blue lines in the images in Figure 3, are illustrated in Figure 4b. Again, for the substrate surface, the photocathodic terraces have high surface potentials (17.5−20 mV), and other terraces have low potentials (11.5−14 mV). Also, the changes in the potential can be correlated with step heights that change the termination. The line traverses six terraces, and from left to right, their heights are 0, 14.7 (13N), 20.2 (18N), 32.6 (29N), 38.1 (34N), and 51.7 Å (46N). The photocathodic terraces are separated by even-N steps which means they have the same composition, and they are separated from the nonphotocathodic terraces by odd-N steps, which therefore have a different composition. The surface roughness of the substrate terraces was also between 0.1 and 0.2 Å. The roughnesses of terraces on the film were ∼1.4 Å, but this does not affect the patterns of reduced silver.

The experiments carried out on the 1 (Figure 2), 2 (Figure S2), 7.5 (Figure 3), and 13 nm thick TiO_2 film (Figure S4) were repeated using a heterostructure consisting of a $SrTiO_3$ (111) substrate and a 25.5 nm thick film. The patterns of silver reduced on the surface of the $SrTiO_3$ (111) substrate and on the surface of the 25.5 nm film at the same location are shown in Figure 5a and 5b, respectively (note the images in Figure 5 are 15 × 15 μm^2). While the 25.5 nm thick film conseals many of the substrate features, it is still possible to locate the traces of large steps and surface scratches. The arrows at the bottom of the images locate equivalent positions on the substrate and film surface. As for all of the substrates, photochemically reduced silver was only found on the terraces that had a higher surface potential (the corresponding KFM image is presented in Figure S5 of the Supporting Information). The pattern of reduced silver on the 25.5 nm thick film does not correlate well with the pattern observed on substrate; instead, there are silver particles relatively evenly distributed across the surface. This result implies that the photochemical reactivity of thicker films (>than 25 nm) is not dominated by the potential difference at the buried substrate−film interface, in contrast to the results for films of thicknesses 1−13 nm.

DOI: 10.1021/acsami.6b16443
ACS Appl. Mater. Interfaces 2017, 9, 7843−7851

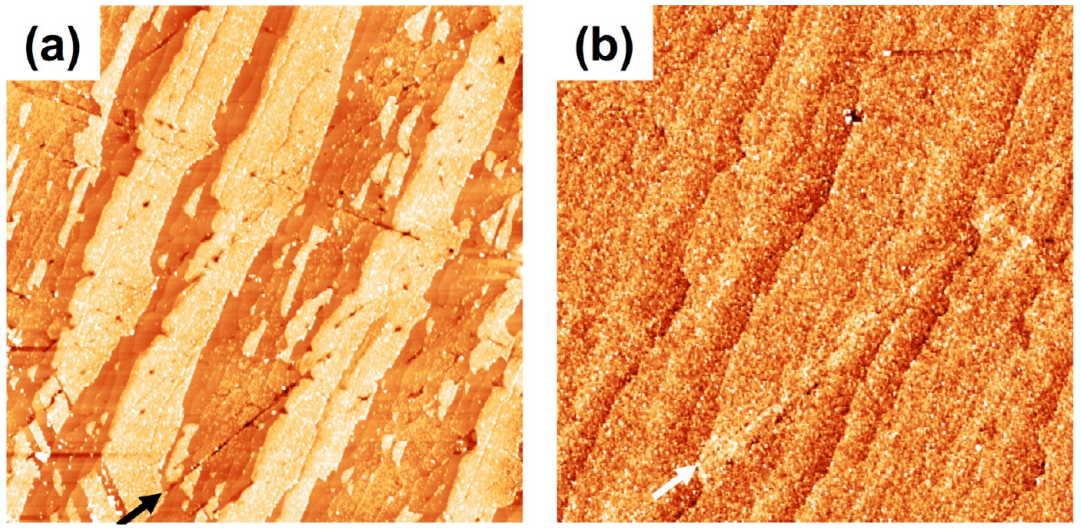

Figure 5. Topographic AFM images of (a) a bare $SrTiO_3$ (111) substrate and the same areas of (b) a 25.5 nm TiO_2 film on the substrate after photoreduction of Ag^+. Both images are 15 μm × 15 μm, and the black-to-white contrast range is 0−15 nm. Arrows mark equivalent locations.

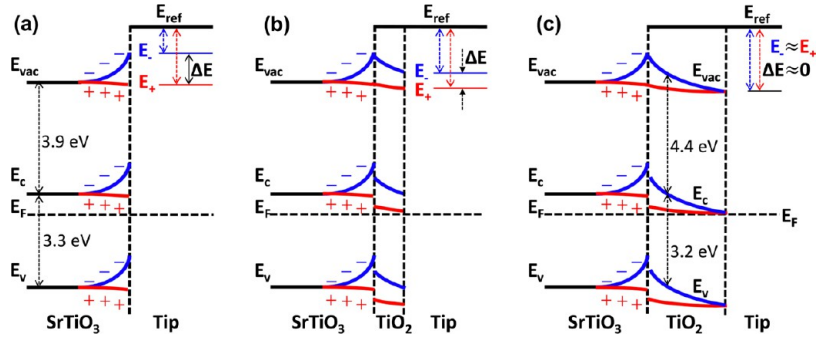

Figure 6. Schematic energy level diagrams of (a) $SrTiO_3$ (111), (b) ultrathin (1 nm) TiO_2 on $SrTiO_3$ (111), and (c) thin TiO_2 (1−13 nm) on $SrTiO_3$ (111), each grounded with PtCr-coated conductive AFM tips. In each, the Fermi levels (E_F) are aligned in all phases while the reference level (E_{ref}) discontinuities between the sample surface and the tip represent the contact potential differences (CPDs) as would be measured by KFM. In each panel, the blue (red) arrows indicate the CPD for photoanodic (photocathodic) terraces. Band bending in the $SrTiO_3$ is affected by the charge on its surface, regardless of whether a film is located on it or not, and controls reactivity in each case.

4. DISCUSSION

The observations in the previous section show that TiO_2 films (up to 13 nm in thickness) supported on $SrTiO_3$ (111) surfaces (which were annealed in air at 1250 °C for 10 h prior to growth) have roughly the same spatially selective reactivity as the bare substrates. For the thinnest film, the relative potential difference between the two terraces is also similar to the potential difference on the bare substrate. These observations indicate that the substrate surface charge is stable with respect to TiO_2 film growth. The charge on the terraces of the bare substrate is trapped at the buried substrate−film interface where it continues to influence the transport of photogenerated electrons and holes.

To understand the mechanism of this phenomenon, we begin by considering where the photoelectrons are generated. $SrTiO_3$ and TiO_2 are both able to reduce Ag when stimulated by UV irradiation,[11,26] but in this experiment the TiO_2 film is too thin to absorb enough light to produce significant concentrations of electron−hole pairs. Because the light used in this experiment has an absorption depth in $SrTiO_3$ and TiO_2 on the order of 10^2 nm,[35−37] the majority of light was adsorbed in the substrate; most of the electrons participating in the silver-reduction reaction must also have been generated in the $SrTiO_3$ substrate. Next, we consider the diffusion length of electrons in TiO_2, which is on the order of 10^2 nm.[38] Because the TiO_2 films were all less than 13 nm thick, the photoelectrons from the substrate can easily get to the film surface by diffusion. Note that because the average terrace width is more than 10 times the film thickness, we assume that carrier diffusion perpendicular to the film influences the reaction more than lateral diffusion. Next, we consider the buried charge. The KFM images measured on the ultrathin film sample show that, after we deposit a 1 nm TiO_2 film on the annealed $SrTiO_3$ (111) substrate, there is still a correlation between surface potential and reactivity, similar to the surface potential and reactivity correlation for bare $SrTiO_3$ (111) substrates. This suggests that the potential difference on the film surface originates from the potential differences of the photocathodic and photoanodic terraces on the buried $SrTiO_3$ (111) surface. Taken together, these considerations indicate that carriers photogenerated in the substrate experience a field from the buried interface charge that attracts different amounts of electrons and holes to the interface, depending on the buried local terrace charge, and some of these carriers traverse the film and react at the TiO_2 surface.

Schematic energy level diagrams are depicted in Figure 6 for (a) the bare $SrTiO_3$ (111) substrate, (b) an ultrathin TiO_2 film

DOI: 10.1021/acsami.6b16443
ACS Appl. Mater. Interfaces 2017, 9, 7843−7851

(~1 nm) on $SrTiO_3$ (111), and (c) thin (1−13 nm) TiO_2 films on $SrTiO_3$ (111), all grounded with a PtCr-coated AFM probe. (Schematic energy level diagrams for $SrTiO_3$, anatase TiO_2, and the PtCr-coated AFM probe before contact can be found in Figure S6 in the Supporting Information.) Both $SrTiO_3$ and TiO_2 are n-type semiconductors, likely owing to oxygen vacancies.[39−41] In the case of a negative (positive) surface or interfacial charge, shown by blue (red) bands, the bands are bent upward (downward) and modify the barrier (field) for electron drift. In other words, the oppositely charged terraces bend the bands in opposite directions. The more (less) negatively charged terraces will have a larger (smaller) barrier to electron drift to the surface/interface and are expected to be less (more) photocathodic. For the $TiO_2/SrTiO_3$ heterostructures, the electrons must traverse the thin TiO_2 layer, either by drift or by diffusion, to participate in surface reactions. This has been shown in recent simulations to have a relatively small influence on the overall reactivity of a terrace.[19,20] In other words, the buried chemical charge of the $SrTiO_3$ surface, which can be controlled through annealing,[12] behaves schematically similar to the buried polar surfaces in ferroelectric heterostructures.

The surface potential value measured by KFM is proportional to the contact potential difference (CPD) between the probe and the sample surface[42,43] and is shown in the schematics of Figure 6 as the discontinuity in the vacuum levels. E_{ref}, E_-, and E_+ denote the vacuum level positions for the AFM tip, photoanodic terraces, and photocathodic terraces, respectively. A negative (positive) surface with upward (downward) band bending results in a smaller (larger) value of the CPD, or the energy difference between E_{ref} and E_- (E_+), and a smaller (larger) measured surface potential. The potential difference between photocathodic and photoanodic terraces is represented as ΔE in Figure 6. For the charged bare substrate surfaces, Figure 6a, and the ultrathin film on the charged substrate surfaces, Figure 6b, where the film is not thick enough to fully screen the substrate charge, one can measure a surface potential difference between the terraces, though the values are smaller for the film than for the bare substrate. As the film thickness is increased, the buried charge is better screened by the film and the band edges for the films are closer to their equilibrium positions, as shown in Figure 6c. In such cases, the CPD (and surface potential) measured for the film above either type of substrate terrace will be similar. It should be noted that in Figure 6c the film is thinner than the space charge region needed to screen the interface charge originating from $SrTiO_3$ polar terminations (thus the TiO_2 bands at the TiO_2/PtCr interface are not bent upward as they would be for bulk n-type TiO_2).[19,20] The experiments can be consistently interpreted according to the schematics in Figure 6, with the substrates similar to Figure 6a, the 1 nm film similar to Figure 6b, and films over 2 nm similar to Figure 6c, even though the exact amount of band bending and the relative differences are not known.

The observation that the spatially selective photochemical reactivity of the substrate can be transferred to a film that normally exhibits spatially uniform reactivity is not completely new. The same phenomenon was observed in $TiO_2/BaTiO_3$ and $TiO_2/BiFeO_3$ heterostructures.[15,17,34] However, while both $BaTiO_3$ and $BiFeO_3$ are ferroelectric, $SrTiO_3$ is not. The observation of this phenomenon in a nonferroelectric material means that it might occur for almost any compound with significant iconicity, rather than only for a limited number of ferroelectrics. For the cases of $BaTiO_3$ and $BiFeO_3$, ferroelectric domains in the bulk with a positive out-of-plane polarization at the surface are photocathodic, while domains with a negative surface polarization are photoanodic.[18] Therefore, the patterns of reduced silver on $BaTiO_3$ and $BiFeO_3$ are correlated with the domain structure. Burbure et al.[15] and Zhang et al.[17] found that thin TiO_2 films supported on $BaTiO_3$ or $BiFeO_3$ substrates photoreduce silver in spatially selective patterns; the patterns of the silver were correlated with the substrate domain structure. The phenomenon is similar for the $TiO_2/SrTiO_3$ heterostructure, except that $SrTiO_3$ is not ferroelectric. We therefore assert that it is the potentials of the polar surface terminations on different buried terraces that influence the motion of photogenerated carriers. In this case, the phenomenon is quite different from a ferroelectric. In the ferroelectric, the polarization arises from the bulk domain structure. Here, it is from the composition of the last layer of the crystal.

While it is not surprising that the addition of a film does not alter the bulk domain structure of a ferroelectric, it is more surprising that the growth of a film does not significantly alter the charge at the surface of the substrate. The reason for this is that the TiO_2 film is not grown on an ideal $SrTiO_3$ (111) surface. The high-temperature annealing that was used to prepare charged terraces on the substrate is likely to create a reconstructed surface region (that may extend several layers below the surface) with varying degrees of Sr deficiency departing from the ideal composition.[12] The film growth occurs at a much lower temperature (700 °C) and does not significantly alter the structure and composition of the $SrTiO_3$ surface layer formed at the higher temperature (1250 °C). Thus, rather than growing on an ideal $SrTiO_3$ substrate, the films examined here grew on a reconstructed, Sr-deficient surface layer. The fact that the TiO_2 films that grow on this surface are polycrystalline and multiphased supports the idea that the high-temperature anneal creates a nonideal growth surface on the substrate. While nonideal for epitaxy, the reconstructed surfaces are stable against growth and their charges are important for the photochemical properties of the heterostructure.

For TiO_2 films supported on $BaTiO_3$ substrates, the buried ferroelectric domains no longer controlled the photochemical reactivity of film surfaces when the film thickness was beyond 50 nm.[15] A computational model of the $TiO_2/BaTiO_3$ heterostructure found that the electron and hole current densities remain the same when the film thickness is beyond ~30 nm, indicating that the photocarriers arriving at the film surface are mainly generated in the film beyond this thickness.[19,20] These observations agree with the observation in this paper that when the thickness of TiO_2 film is increased (here to 25.5 nm), the photochemical reactivity of films supported on photocathodic and photoanodic terraces become similar, as more photoelectrons are photogenerated in the TiO_2 layer. The diffusion length of electrons in TiO_2 is greater than 100 nm,[38] though the diffusion length in polycrystalline films should be smaller than this. Some combination between decreased driving forces and small diffusion lengths leads to the disappearance of substrate-induced spatial selectivity at thicknesses between 13 and 25.5 nm.

It should be noted that earlier studies showed that $TiO_2/SrTiO_3$ composites had enhanced UV light photocatalytic activity compared to the separated phases.[21,24] In the $TiO_2/SrTiO_3$ heterostructures described here, we also observed slightly enhanced photoreactivity for the reduction of silver.

DOI: 10.1021/acsami.6b16443
ACS Appl. Mater. Interfaces 2017, 9, 7843−7851

Films supported on originally unreactive $SrTiO_3$ terraces (photoanodic) reduced some silver, while films supported on photocathodic $SrTiO_3$ terraces were just as reactive as the bare surface. This is understandable because TiO_2 is a good photocatalyst when activated by UV light. Although the film is thin, it still absorbs some light and produces photocarriers to participate in the reaction. It should also be noted that the electronic structure of the heterostructure can promote the separation of photogenerated charge carriers. Because both the conduction band and the valence band of $SrTiO_3$ are at higher energies than the comparable bands in TiO_2 (as depicted in Figure 6 and Figure S6)[44−46] photogenerated electrons in $SrTiO_3$ can reduce their energy by moving to the conduction band of TiO_2 and ultimately to the surface to reduce Ag^+ from solution.

The findings reported here might ultimately have an important impact on the design of photocatalysts. The idea of using fixed charges on catalyst surfaces to separate photogenerated carriers, ameliorate recombination, and increase reaction efficiency is well established.[47−51] By burying these charges at an internal interface covered by TiO_2, the catalyst will be stable in an aqueous environment and the charges will be protected from degradation. While this has been demonstrated before for TiO_2-coated ferroelectrics,[15,17,21] $SrTiO_3$ offers a significant possible advantage compared to ferroelectrics because the ratio of photocathodic to photoanodic surface area can be controlled.[12] The relative areas of the polar domains on the surface of a ferroelectric are nearly equal. The best ratio for the areas of the photocathodic and photoanodic surfaces is the one that maximizes the overall reaction rate. This is presumably the inverse of the ratio of the area specific rates of the cathodic and anodic half reactions, and this is unlikely to be unity. While the ratios of opposite domains can be controlled in bulk ferroelectrics by poling, it is not clear how this could be accomplished with a powdered catalyst. However, we have recently demonstrated that the ratio of photocathodic and photoanodic surface area on the $SrTiO_3$ (111) surface can be controlled by high-temperature thermal treatments.[12] Therefore, it is possible, at least in principle, to create catalysts with controlled distributions of surfaces promoting photocathodic or photoanodic reactions and to protect these surfaces with a thin TiO_2 layer that also preserves the benefits associated with charge carrier separation.

5. CONCLUSIONS

When silver is photochemically reduced on thin (≤13 nm) TiO_2 films supported by $SrTiO_3$ (111) substrates, the pattern of silver on the film surface mimics the pattern that is reduced on the substrate surface before the film is deposited. Silver is preferentially reduced above terraces that have a more positive surface potential than the unreactive terraces. These observations indicate that the charges on different terraces on the $SrTiO_3$ (111) surface remain at the buried interface after film growth. At the interface, they influence the transport of photogenerated charge carriers to the surface such that silver is reduced on the film above the photocathodic terraces on the substrate.

■ ASSOCIATED CONTENT

Supporting Information

The Supporting Information is available free of charge on the ACS Publications website at DOI: 10.1021/acsami.6b16443.

Additional scanning probe microscopy data from 1, 2, 7.5, 13, and 25.5 nm thick films, and proposed energy level diagrams for the heterostructures (PDF)

■ AUTHOR INFORMATION

Corresponding Author

*E-mail: gr20@andrew.cmu.edu.

ORCID

Gregory S. Rohrer: 0000-0002-9671-3034

Notes

The authors declare no competing financial interest.

■ ACKNOWLEDGMENTS

We acknowledge the support of the National Science Foundation grant DMR 1609369 and use of the Materials Characterization Facility at Carnegie Mellon University supported by grant MCF-677785.

■ REFERENCES

(1) Yang, J.; Wang, J.; Li, X.; Lang, J.; Liu, F.; Yang, L.; Zhai, H.; Gao, M.; Zhao, X. Effect of Polar and Non-Polar Surfaces of ZnO Nanostructures on Photocatalytic Properties. *J. Alloys Compd.* **2012**, *528*, 28−33.

(2) Bae, H.; Kim, E.; Park, J.-B.; Kang, S.-J.; Fujii, K.; Lee, S. H.; Lee, H.-J.; Ha, J.-S. Effect of Polarity on Photoelectrochemical Properties of Polar and Semipolar GaN Photoanode. *J. Electrochem. Soc.* **2016**, *163*, H213−H217.

(3) Lehn, J. M.; Sauvage, J. P.; Ziessel, R. Photochemical Water Splitting Continuous Generation of Hydrogen and Oxygen by Irradiation of Aqueous Suspensions of Metal Loaded Strontium-Titanate. *New J. Chem.* **1980**, *4*, 623−627.

(4) Luo, J. H.; Maggard, P. A. Hydrothermal Synthesis and Photocatalytic Activities of $SrTiO_3$-Coated Fe_2O_3 and $BiFeO_3$. *Adv. Mater.* **2006**, *18*, 514−517.

(5) Townsend, T. K.; Browning, N. D.; Osterloh, F. E. Nanoscale Strontium Titanate Photocatalysts for Overall Water Splitting. *ACS Nano* **2012**, *6*, 7420−7426.

(6) Chiaramonti, A. N.; Lanier, C. H.; Marks, L. D.; Stair, P. C. Time, Temperature, and Oxygen Partial Pressure-Dependent Surface Reconstructions on $SrTiO_3$(111): A Systematic Study of Oxygen-Rich Conditions. *Surf. Sci.* **2008**, *602*, 3018−3025.

(7) Marks, L. D.; Chiaramonti, A. N.; Tran, F.; Blaha, P. The Small Unit Cell Reconstructions of $SrTiO_3$(111). *Surf. Sci.* **2009**, *603*, 2179−2187.

(8) Russell, B. C.; Castell, M. R. Surface of Sputtered and Annealed Polar $SrTiO_3$(111): TiO_x-Rich (*N* X *N*) Reconstructions. *J. Phys. Chem. C* **2008**, *112*, 6538−6545.

(9) Ferrer, S.; Somorjai, G. A. UPS and XPS Studies of Chemisorption of O_2, H_2, and H_2O on Reduced and Stoichiometric $SrTiO_3$(111) Surfaces - the Effects of Illumination. *Surf. Sci.* **1980**, *94*, 41−56.

(10) Nagarkar, P. V.; Searson, P. C.; Gealy, F. D. Effect of Surface-Treatment on $SrTiO_3$ - an X-Ray Photoelectron Spectroscopic Study. *J. Appl. Phys.* **1991**, *69*, 459−462.

(11) Giocondi, J. L.; Rohrer, G. S. Structure Sensitivity of Photochemical Oxidation and Reduction Reactions on $SrTiO_3$ Surfaces. *J. Am. Ceram. Soc.* **2003**, *86*, 1182−1189.

(12) Zhu, Y.; Salvador, P. A.; Rohrer, G. S. Controlling the Relative Areas of Photocathodic and Photoanodic Terraces on the $SrTiO_3$(111) Surface. *Chem. Mater.* **2016**, *28*, 5155−5162.

(13) Goniakowski, J.; Finocchi, F.; Noguera, C. Polarity of Oxide Surfaces and Nanostructures. *Rep. Prog. Phys.* **2008**, *71*, 016501.

(14) Tasker, P. W. Stability of Ionic-Crystal Surfaces. *J. Phys. C: Solid State Phys.* **1979**, *12*, 4977−4984.

DOI: 10.1021/acsami.6b16443
ACS Appl. Mater. Interfaces 2017, 9, 7843−7851

(15) Burbure, N. V.; Salvador, P. A.; Rohrer, G. S. Photochemical Reactivity of Titania Films on $BaTiO_3$ Substrates: Origin of Spatial Selectivity. *Chem. Mater.* **2010**, *22*, 5823−5830.
(16) Heller, A. Chemistry and Applications of Photocatalytic Oxidation of Thin Organic Films. *Acc. Chem. Res.* **1995**, *28*, 503−508.
(17) Zhang, Y. L.; Schultz, A. M.; Salvador, P. A.; Rohrer, G. S. Spatially Selective Visible Light Photocatalytic Activity of TiO_2/$BiFeO_3$ Heterostructures. *J. Mater. Chem.* **2011**, *21*, 4168−4174.
(18) Giocondi, J. L.; Rohrer, G. S. Spatial Separation of Photochemical Oxidation and Reduction Reactions on the Surface of Ferroelectric $BaTiO_3$. *J. Phys. Chem. B* **2001**, *105*, 8275−8277.
(19) Glickstein, J. J.; Salvador, P. A.; Rohrer, G. S. Computational Model of Domain-Specific Reactivity on Coated Ferroelectric Photocatalysts. *J. Phys. Chem. C* **2016**, *120*, 12673−12684.
(20) Glickstein, J. J.; Salvador, P. A.; Rohrer, G. S. Multidomain Simulations of Coated Ferroelectrics Exhibiting Spatially Selective Photocatalytic Activity with High Internal Quantum Efficiencies. *J. Mater. Chem. A* **2016**, *4*, 16085−16093.
(21) Li, L.; Rohrer, G. S.; Salvador, P. A. Heterostructured Ceramic Powders for Photocatalytic Hydrogen Production: Nanostructured TiO_2 Shells Surrounding Microcrystalline (Ba,Sr)TiO_3 Cores. *J. Am. Ceram. Soc.* **2012**, *95*, 1414−1420.
(22) Hirano, M.; Nakahara, C.; Ota, K.; Inagaki, M. Direct Formation of Zirconia-Doped Titania with Stable Anatase-Type Structure by Thermal Hydrolysis. *J. Am. Ceram. Soc.* **2002**, *85*, 1333−1335.
(23) Inagaki, M.; Nakazawa, Y.; Hirano, M.; Kobayashi, Y.; Toyoda, M. Preparation of Stable Anatase-Type TiO_2 and Its Photocatalytic Performance. *Int. J. Inorg. Mater.* **2001**, *3*, 809−811.
(24) Zhang, J.; Bang, J. H.; Tang, C.; Kamat, P. V. Tailored TiO_2-$SrTiO_3$ Heterostructure Nanotube Arrays for Improved Photoelectrochemical Performance. *ACS Nano* **2010**, *4*, 387−395.
(25) Necas, D.; Klapetek, P. Gwyddion: An Open-Source Software for SPM Data Analysis. *Cent. Eur. J. Phys.* **2012**, *10*, 181−188.
(26) Lowekamp, J. B.; Rohrer, G. S.; Morris Hotsenpiller, P. A.; Bolt, J. D.; Farneth, W. E. Anisotropic Photochemical Reactivity of Bulk TiO_2 Crystals. *J. Phys. Chem. B* **1998**, *102*, 7323−7327.
(27) Munprom, R.; Salvador, P. A.; Rohrer, G. S. Polar Domains at the Surface of Centrosymmetric $BiVO_4$. *Chem. Mater.* **2014**, *26*, 2774−2776.
(28) Herrmann, J. M.; Disdier, J.; Pichat, P. Photocatalytic Deposition of Silver on Powder Titania - Consequences for the Recovery of Silver. *J. Catal.* **1988**, *113*, 72−81.
(29) Burbure, N. V.; Salvador, P. A.; Rohrer, G. S. Orientation and Phase Relationships between Titania Films and Polycrystalline $BaTiO_3$ Substrates as Determined by Electron Backscatter Diffraction Mapping. *J. Am. Ceram. Soc.* **2010**, *93*, 2530−2533.
(30) Wyckoff, R. W. G. *Crystal Structures*; Interscience: New York, 1964; Vol. 2.
(31) Cromer, D. T.; Herrington, K. The Structures of Anatase and Rutile. *J. Am. Chem. Soc.* **1955**, *77*, 4708−4709.
(32) Lotnyk, A.; Senz, S.; Hesse, D. Epitaxial Growth of TiO_2 Thin Films on $SrTiO_3$, $LaAlO_3$ and Yttria-Stabilized Zirconia Substrates by Electron Beam Evaporation. *Thin Solid Films* **2007**, *515*, 3439−3447.
(33) *X'pert Pro Mrd Xl: Pw3217 X'pert Reflectivity*; PANalytical: The Netherlands, 2007.
(34) Burbure, N. V.; Salvador, P. A.; Rohrer, G. S. Photochemical Reactivity of Titania Films on $BaTiO_3$ Substrates: Influence of Titania Phase and Orientation. *Chem. Mater.* **2010**, *22*, 5831−5837.
(35) Frye, A.; French, R. H.; Bonnell, D. A. Optical Properties and Electronic Structure of Oxidized and Reduced Single-Crystal Strontium Titanate. *Z. Metallkd.* **2003**, *94*, 226−232.
(36) Sekiya, T.; Ichimura, K.; Igarashi, M.; Kurita, S. Absorption Spectra of Anatase TiO_2 Single Crystals Heat-Treated under Oxygen Atmosphere. *J. Phys. Chem. Solids* **2000**, *61*, 1237−1242.
(37) Tang, H.; Levy, F.; Berger, H.; Schmid, P. E. Urbach Tail of Anatase TiO_2. *Phys. Rev. B: Condens. Matter Mater. Phys.* **1995**, *52*, 7771−7774.
(38) Yamada, Y.; Kanemitsu, Y. Determination of Electron and Hole Lifetimes of Rutile and Anatase TiO_2 Single Crystals. *Appl. Phys. Lett.* **2012**, *101*, 133907.
(39) Breckenridge, R. G.; Hosler, W. R. Electrical Properties of Titanium Dioxide Semiconductors. *Phys. Rev.* **1953**, *91*, 793−802.
(40) Forro, L.; Chauvet, O.; Emin, D.; Zuppiroli, L.; Berger, H.; Levy, F. High-Mobility n-Type Charge-Carriers in Large Single-Crystals of Anatase (TiO_2). *J. Appl. Phys.* **1994**, *75*, 633−635.
(41) Robertson, J.; Chen, C. W. Schottky Barrier Heights of Tantalum Oxide, Barium Strontium Titanate, Lead Titanate, and Strontium Bismuth Tantalate. *Appl. Phys. Lett.* **1999**, *74*, 1168−1170.
(42) Melitz, W.; Shen, J.; Kummel, A. C.; Lee, S. Kelvin Probe Force Microscopy and Its Application. *Surf. Sci. Rep.* **2011**, *66*, 1−27.
(43) Nonnenmacher, M.; O'Boyle, M. P.; Wickramasinghe, H. K. Kelvin Probe Force Microscopy. *Appl. Phys. Lett.* **1991**, *58*, 2921−2923.
(44) Pan, J.; Liu, G.; Lu, G. Q.; Cheng, H.-M. On the True Photoreactivity Order of {001}, {010}, and {101} Facets of Anatase TiO_2 Crystals. *Angew. Chem., Int. Ed.* **2011**, *50*, 2133−2137.
(45) Thomas, A. G.; Flavell, W. R.; Mallick, A. K.; Kumarasinghe, A. R.; Tsoutsou, D.; Khan, N.; Chatwin, C.; Rayner, S.; Smith, G. C.; Stockbauer, R. L.; Warren, S.; Johal, T. K.; Patel, S.; Holland, D.; Taleb, A.; Wiame, F. Comparison of the Electronic Structure of Anatase and Rutile TiO_2 Single-Crystal Surfaces Using Resonant Photoemission and X-Ray Absorption Spectroscopy. *Phys. Rev. B: Condens. Matter Mater. Phys.* **2007**, *75*, 035105.
(46) van Benthem, K.; Elsasser, C.; French, R. H. Bulk Electronic Structure of $SrTiO_3$: Experiment and Theory. *J. Appl. Phys.* **2001**, *90*, 6156−6164.
(47) Batzill, M. Fundamental Aspects of Surface Engineering of Transition Metal Oxide Photocatalysts. *Energy Environ. Sci.* **2011**, *4*, 3275−3286.
(48) Kakekhani, A.; Ismail-Beigi, S. Ferroelectric-Based Catalysis: Switchable Surface Chemistry. *ACS Catal.* **2015**, *5*, 4537−4545.
(49) Khan, M. A.; Nadeem, M. A.; Idriss, H. Ferroelectric Polarization Effect on Surface Chemistry and Photo-Catalytic Activity: A Review. *Surf. Sci. Rep.* **2016**, *71*, 1−31.
(50) Li, L.; Salvador, P. A.; Rohrer, G. S. Photocatalysts with Internal Electric Fields. *Nanoscale* **2014**, *6*, 24−42.
(51) Tiwari, D.; Dunn, S. Photochemistry on a Polarisable Semi-Conductor: What Do We Understand Today? *J. Mater. Sci.* **2009**, *44*, 5063−5079.

DOI: 10.1021/acsami.6b16443
ACS Appl. Mater. Interfaces 2017, 9, 7843−7851

Supplemental Information for:

Buried charge at the $TiO_2/SrTiO_3$ (111) interface and its effect on photochemical reactivity

Yisi Zhu, Paul A. Salvador, and Gregory S. Rohrer*

Carnegie Mellon University, Department of Materials Science and Engineering, Pittsburgh, PA 15213

*corresponding author email address: gr20@andrew.cmu.edu

1) 1 nm thick TiO_2 film on $SrTiO_3$ (111)

Figure S1 presents additional, larger area (15 x 15 μm^2) images of the sample already described in Figure 2 of the main text (which showed 5 x 5 μm^2 images). The blue boxes in Fig. S1 (a) and (d) illustrate the area where the higher resolution images presented in Fig. 2 were recorded. These images demonstrate that all of the trends found in Fig. 2 occur over a larger area.

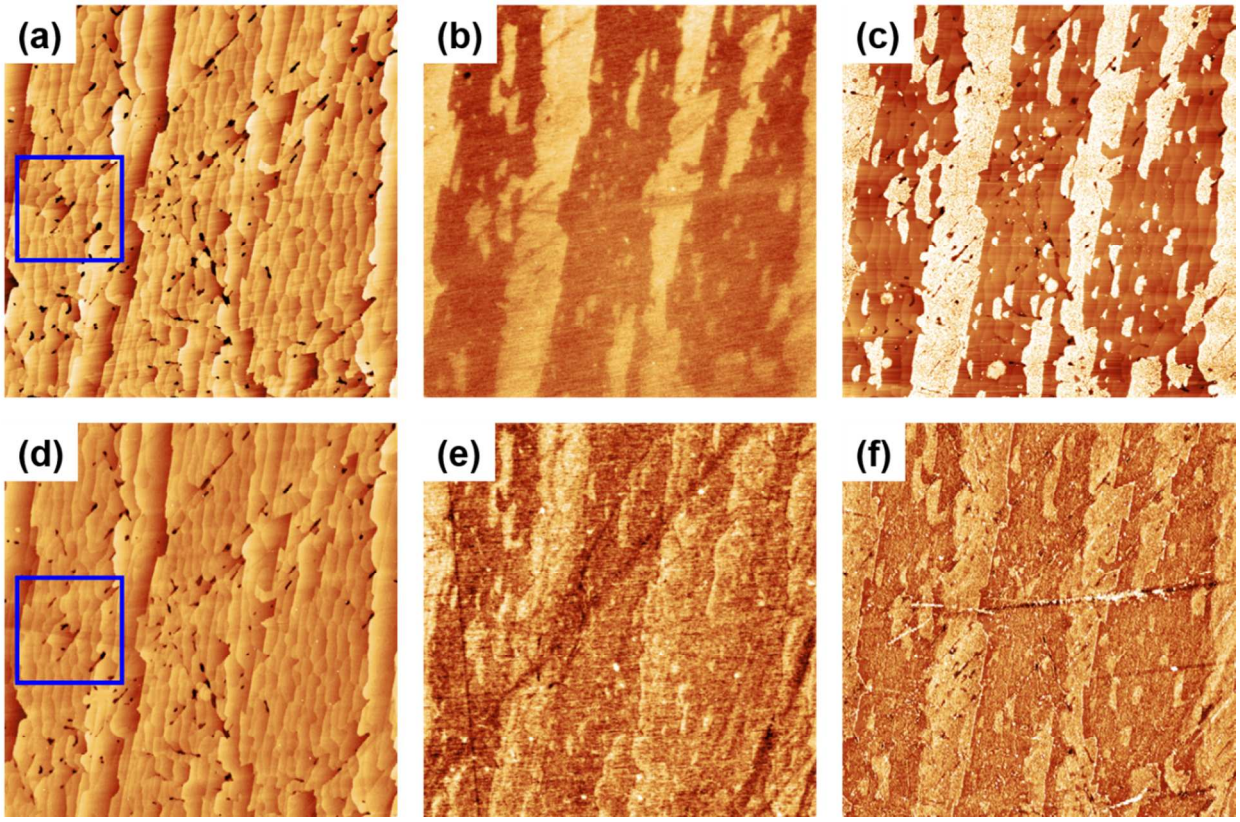

Figure S1. (a,d) Topographic AFM images and (b,e) surface potential images before the reaction, and (c,f) topographic images of the same areas after the photochemical reduction of Ag^+. (a-c) Images of a bare $SrTiO_3$ surface and (d-f) a 1 nm thick TiO_2 film surface supported on the same $SrTiO_3$ (111) substrate at the same location. The field of view for all images is 15 μm × 15 μm. In these images, the black-to-white contrast range is: (a,d) 0 – 5 nm, (b) 0 – 30 mV, (e) 0 – 20 mV, and (c,f) 0 – 10 nm.

2) 2 nm thick TiO_2 film on $SrTiO_3$ (111)

The main text described in detail experiments carried out on 1 nm thick and 7.5 nm thick TiO_2 films on $SrTiO_3$ (111). Parallel experiments were also carried out on a sample with a 2 nm

thick TiO_2 film and the results are presented in Fig. S2. The results of this experiment are consistent with and reinforce the results of the experiment on the 7.5 nm thick film. There is, however, one topographic feature in the images in S2 that is not found in the other experiments. Specifically, slip traces from dislocation activity are present along the [110] direction and are marked with a blue line in Fig. S2(a) and (d). This is an unintended artifact of the experimental procedure. To locate the same area in repeated experiments, a diamond scribe was used to make fiducial marks on the surfaces. Deformation associated with the scribing process generates dislocations in the area of the scratch. These dislocations can migrate out of the crystal during handling, cleaning, and while being heating during film growth. When a dislocation exits the crystal, it leaves a slip step at the intersection of the surface and the slip plane. Normally we avoid the area near the scratch so these traces are not found in any of the other images. However, in this experiment, we inadvertently characterized an area that was too close to the site of damage and the slip steps are visible. Unlike the structural surface steps, these steps do not change the termination. Other than these slip steps, the images of the substrate and the film share all of the characteristics of those presented in Fig. 3 and later in Figs. S3 and S4.

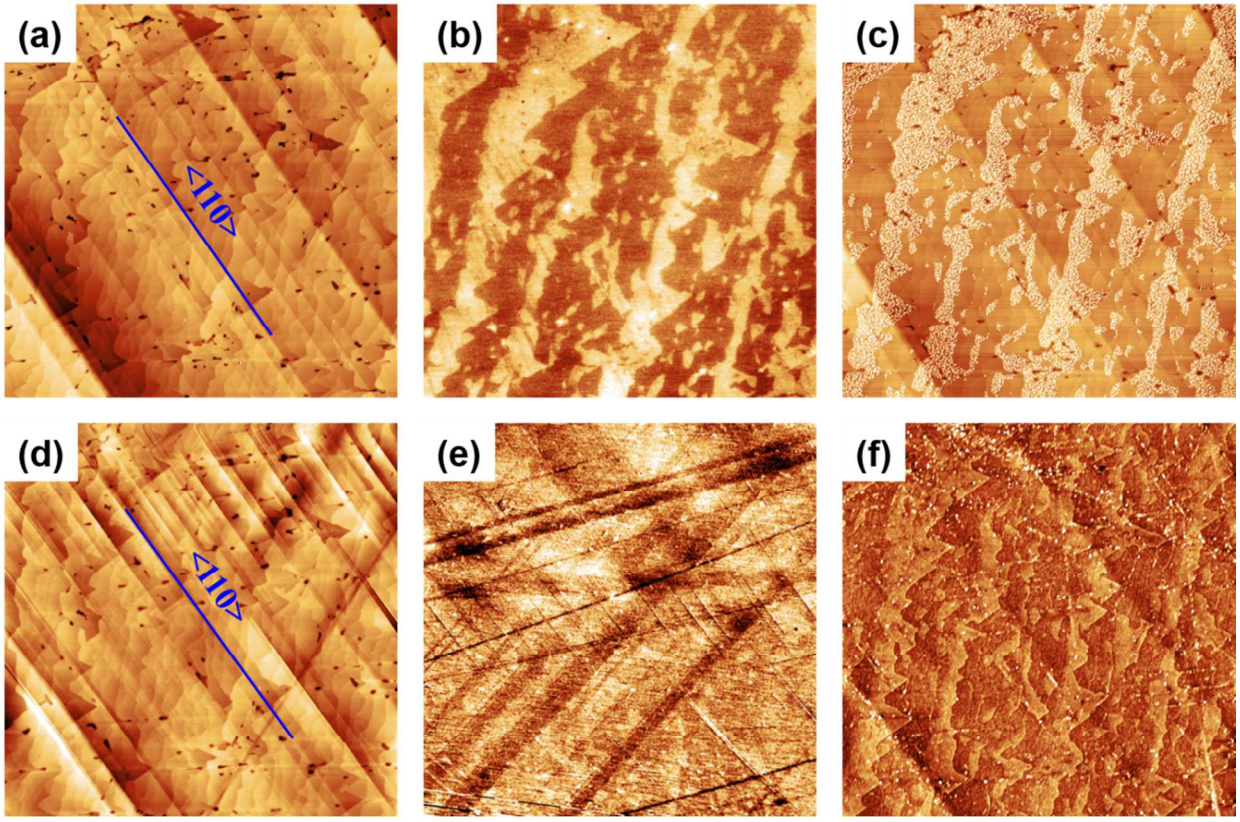

Figure S2. (a,d) Topographic AFM images, (b,e) surface potential images of the clean surfaces, and (c,f) topographic images of the same areas after the photochemical reduction of Ag^{+}. (a-c) Images of a bare $SrTiO_3$ surface and (d-f) a 2 nm thick TiO_2 film surface supported on the same $SrTiO_3$ (111) substrate and at the same location. Blue lines in (a) and (d) indicate slip traces along the <110> direction, generated from dislocations that migrate out of the crystal during handling and the heating experienced during film growth. All images are 15 μm × 15 μm. The contrast range from black-to-white is: (a,d) 0 – 5 nm, (b) 0 – 30 mV, (e) 0 – 20 mV, and (c,f) 0 – 10 nm.

3) 7.5 nm thick TiO_2 film on $SrTiO_3$ (111)

Figure S3 presents additional, larger area (15 x 15 μm^2) images of the sample already described in Figure 3 of the main text (which showed 5 x 5 μm^2 images). The blue boxes in Fig. S3 (a) and (d) illustrate the area where the higher resolution images presented in Fig. 3 were recorded. These images demonstrate that all of the trends found in Fig. 3 occur over a larger area.

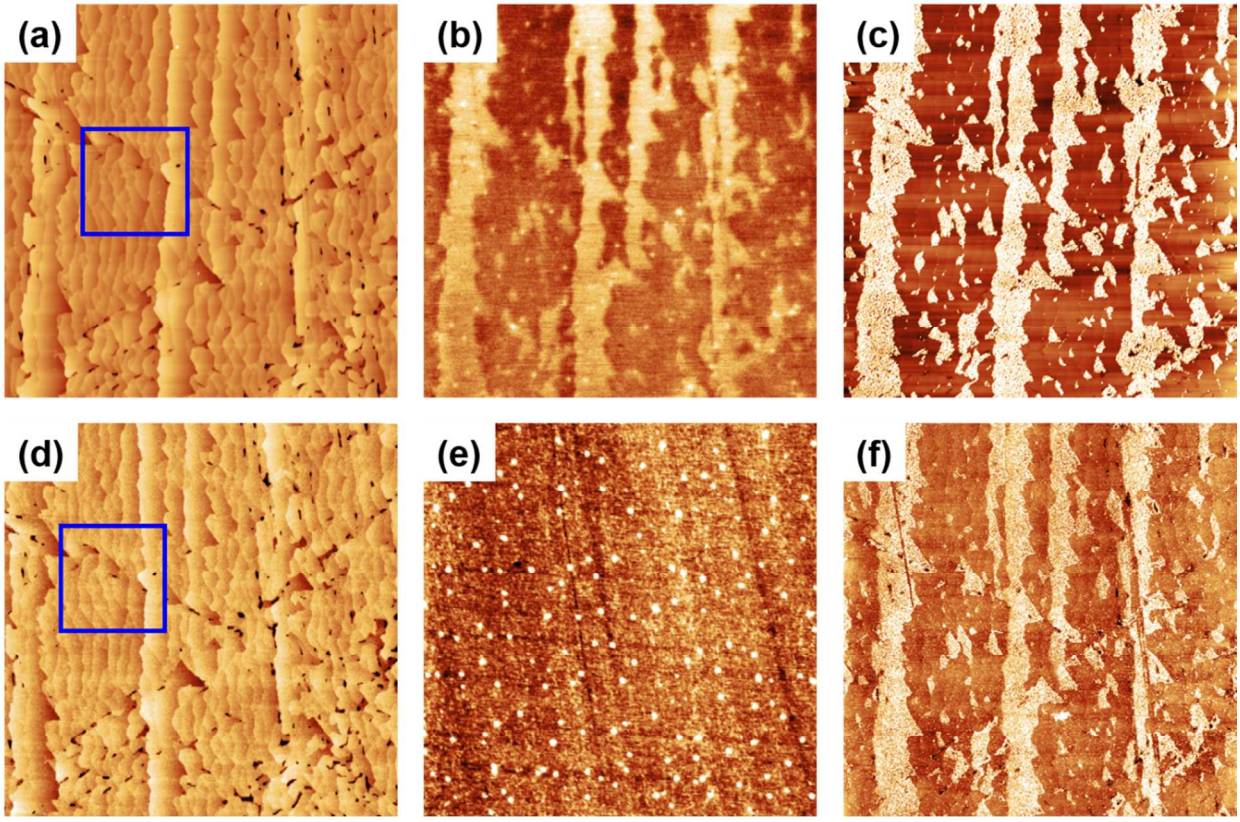

Figure S3. (a,d) Topographic AFM images, (b,e) surface potential images of clean surfaces, and (c,f) topographis images after the photochemical reduction of Ag^{+} at the same location. (a-c) Images of a bare $SrTiO_3$ surface and (d-f) a 7.5 nm thick TiO_2 film surface supported on the same $SrTiO_3$ (111) substrate and at the same location. Blue boxes in (a) and (d) mark the same location that was presented in Fig. 3. All images are 15 μm × 15 μm. The contrast range from black-to-white is: (a,d) 0 – 5 nm, (b) 0 – 25 mV, (e) 0 – 20 mV, and (c,f) 0 – 10 nm.

4) 13 nm thick TiO_2 film on $SrTiO_3$ (111)

The main text described in detail experiments carried out on 1 nm thick and 7.5 nm thick TiO_2 films on $SrTiO_3$ (111). Parallel experiments were also carried out on a sample with a 13 nm thick TiO_2 film and the results are presented in Fig. S4. The results of this experiment are consistent with and reinforce the results of the experiment on the 2 and 7.5 nm thick films; the surface potential contrast observed on the substrate is not present for the film (Fig. S4 (b) and (e)), but the pattern of photochemically reduced silver on the film surface is still similar to the

pattern produced on bare substrate. These results reinforce the points made in the main text, but demonstrate the effects over a much larger area of a 13 nm thick film.

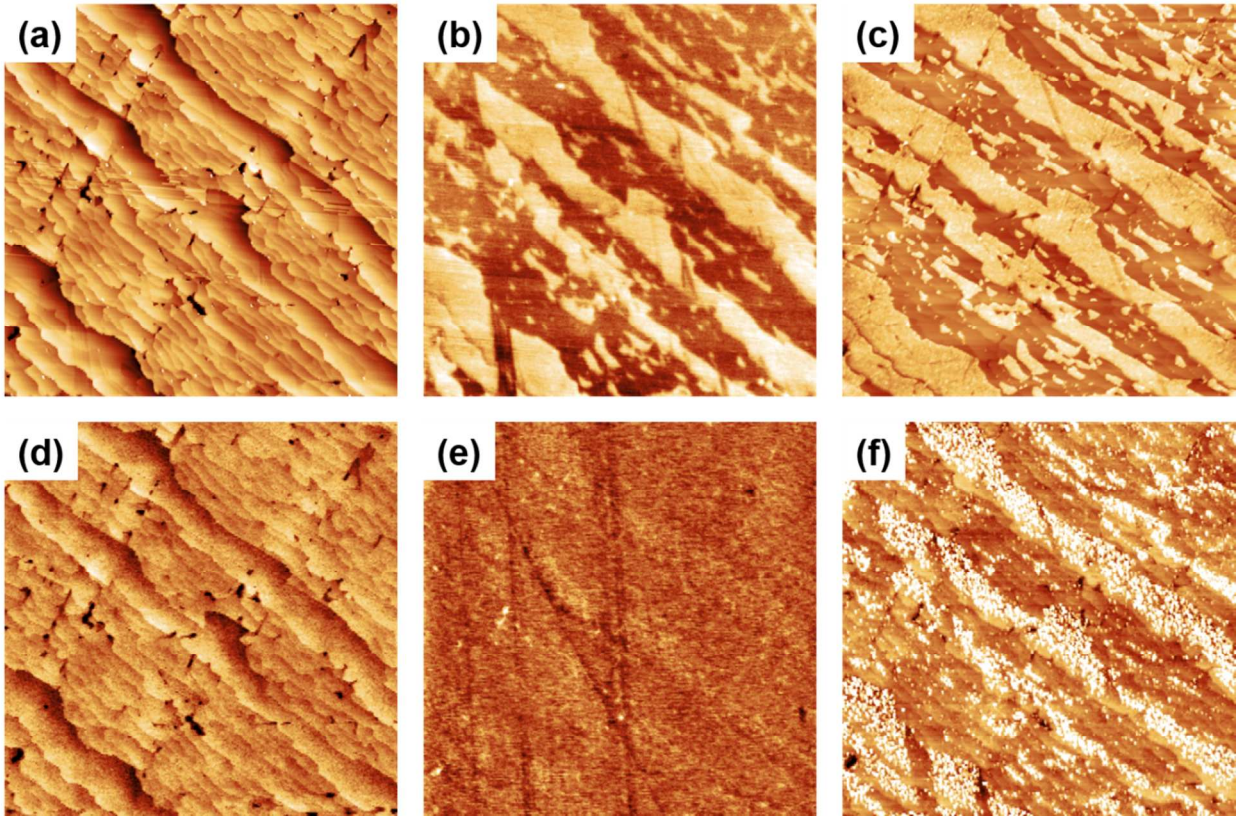

Figure S4. (a,d) Topographic AFM images and (b,e) surface potential images of the clean surfaces, and (c,f) topographic images after the photochemical reduction of Ag^{+} at the same location. (a-c) Images of the bare $SrTiO_3$ surface and (d-f) a 13 nm thick TiO_2 film surface supported on the same $SrTiO_3$ (111) substrate and at the same location. All images are 15 μm × 15 μm. The contrast range from black-to-white is: (a,d) 0 – 5 nm, (b) 0 – 40 mV, (e) 0 – 30 mV, and (c,f) 0 – 10 nm.

5) 25.5 nm thick TiO_2 film on $SrTiO_3$ (111)

The main text described in detail experiments carried out on 1 nm thick and 7.5 nm thick TiO_2 films on $SrTiO_3$ (111). Parallel experiments were also carried out on a sample with a 25.5 nm thick TiO_2 film and two images were presented in Fig. 5 in the main text. For completeness, the remaining images from the experiment are presented in Fig. S5. Note that the images in Fig. S5(c) and (f) the same ones already presented in Fig. 5 of the main text. Similar to the

previously discussed experiments with films thicker than 1 nm, the surface potential contrast present for the substrate is not present for the film. Unlike the films of thicknesses ≤ 13 nm, the spatially selective photochemical reactivity observed for the substrate is absent for the 22.5 nm thick film, indicating the photochemical reactivity of the film surface is no longer influenced by the buried charge.

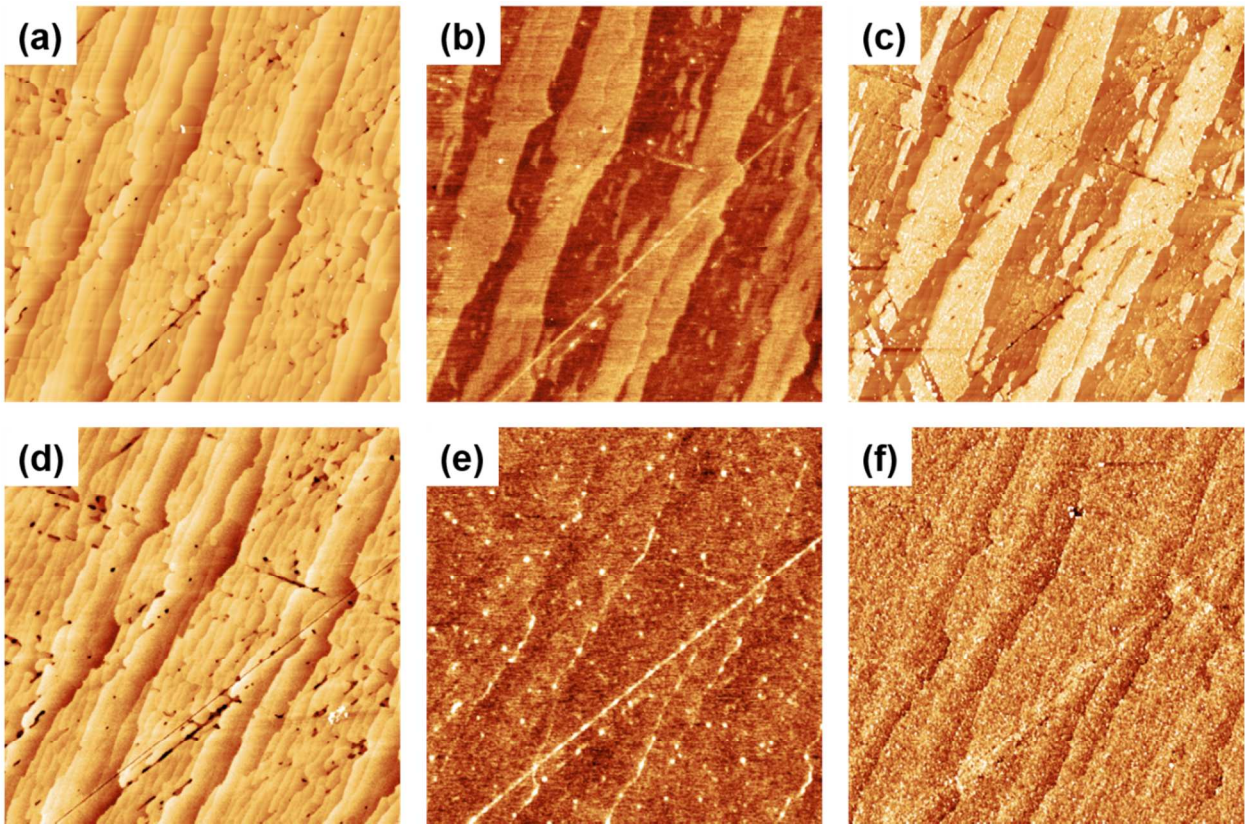

Figure S5. (a,d) Topographic AFM images, (b,e) surface potential images of the clean surfaces, and (c,f) topographic images after the photochemical reduction of Ag^+ at the same location. (a-c) Images of a bare $SrTiO_3$ surface and (d-f) a 22.5 nm thick TiO_2 film surface supported on the same $SrTiO_3$ (111) substrate and at the same location. All images are 15 μm × 15 μm. The contrast range from black-to-white is: (a,d) 0 – 5 nm, (b) 0 – 30 mV, (e) 0 – 20 mV, and (c,f) 0 – 10 nm.

6) Energy level diagrams of $SrTiO_3$, TiO_2, and the AFM probe before and after contact

The pre-contact (flat-band) energy level diagrams for $SrTiO_3$, TiO_2, and the AFM probe are depicted in Fig. S6(a). For $SrTiO_3$, the electron affinity is estimated to be 3.9 eV,[1] which is the

energy between the vacuum level (E_{vac}) and the conduction band edge, E_c. The band gap is ≈ 3.3 eV, which is an average from several reported values.[1-3] Finally, the Fermi level is estimated to be ≈ 0.7 eV below the bottom of the conduction band.[1] For anatase TiO_2, the electron affinity is ≈ 4.4 eV,[4] the band gap is ≈ 3.2 eV,[5, 6] and the Fermi level is only 4.2×10^{-3} eV below the conduction band.[7] For the Pt/Cr coated AFM probe, the work function is estimated to be ≈ 5.07 eV which is the average of the work function of Pt (5.64 eV) and Cr (4.5 eV).[8-10]

A schematic band diagram for a $SrTiO_3$ / anatase TiO_2 heterostructure, with a very thick (> 100 nm) TiO_2 layer that allows for the TiO_2 bands to relax away from the interfaces to the equilibrium values, in contact with the Pt/Cr tip, is shown in Fig. S6(b). At the interface between $SrTiO_3$ and TiO_2, when the Fermi levels are aligned in equilibrium, the $SrTiO_3$ has downward band bending and TiO_2 has upward band bending (here we assume no interface charges are present). We also assume the TiO_2 has upward band bending at the TiO_2/Tip (or a TiO_2/$AgNO_3$ (aq)) interface, as is generally observed for n-type material from surface effects. Note the vacuum level (E_{vac}) discontinuity at this interface denotes the contact potential difference that would be measured by KFM.

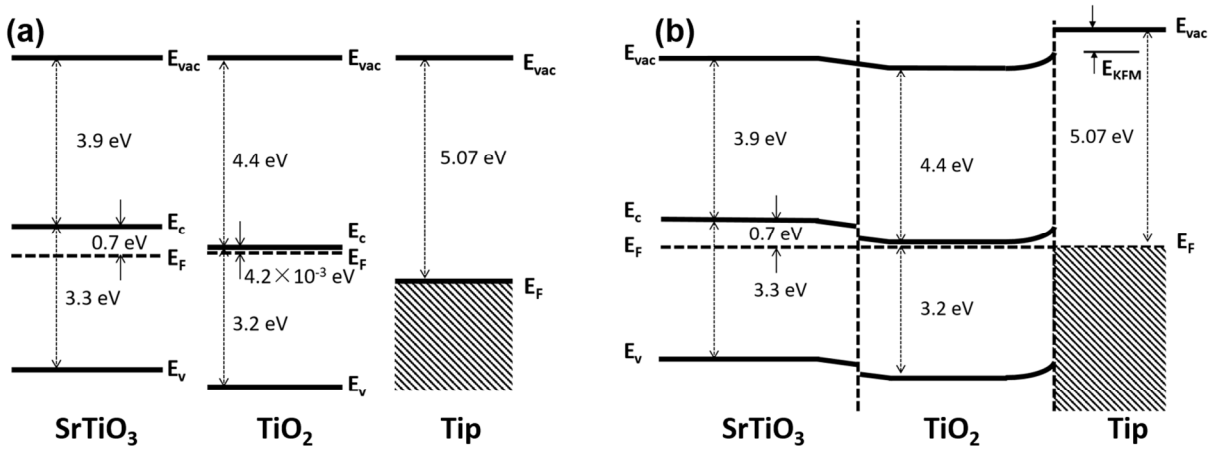

Figure S6. Schematic energy level diagrams of $SrTiO_3$, TiO_2, and a Pt/Cr coated AFM probe (a) before and (b) after contacting the oxides and grounding them to the tip. For each, E_{vac} is the vacuum level energy, E_c is the conduction band edge energy, E_v is the valence band edge energy, and the E_F is the Fermi level energy. E_{KFM} indicates the potential measured at surface.

References:

1. Robertson, J.; Chen, C. W., Schottky Barrier Heights of Tantalum Oxide, Barium Strontium Titanate, Lead Titanate, and Strontium Bismuth Tantalate. *Appl. Phys. Lett.* **1999,** 74, 1168-1170.
2. van Benthem, K.; Elsasser, C.; French, R. H., Bulk Electronic Structure of $SrTiO_3$: Experiment and Theory. *J. Appl. Phys.* **2001,** 90, 6156-6164.
3. Bao, D. H.; Yao, X.; Wakiya, N.; Shinozaki, K.; Mizutani, N., Band-Gap Energies of Sol-Gel-Derived $SrTiO_3$ Thin Films. *Appl. Phys. Lett.* **2001,** 79, 3767-3769.
4. Lenzmann, F.; Krueger, J.; Burnside, S.; Brooks, K.; Gratzel, M.; Gal, D.; Ruhle, S.; Cahen, D., Surface Photovoltage Spectroscopy of Dye-Sensitized Solar Cells with TiO_2, Nb_2O_5, and $SrTiO_3$ Nanocrystalline Photoanodes: Indication for Electron Injection from Higher Excited Dye States. *J. Phys. Chem. B* **2001,** 105, 6347-6352.
5. Tang, H.; Berger, H.; Schmid, P. E.; Levy, F., Optical-Properties of Anatase (TiO_2). *Solid State Comm.* **1994,** 92, 267-271.
6. Tang, H.; Levy, F.; Berger, H.; Schmid, P. E., Urbach Tail of Anatase TiO_2. *Phys. Rev. B* **1995,** 52, 7771-7774.
7. Forro, L.; Chauvet, O.; Emin, D.; Zuppiroli, L.; Berger, H.; Levy, F., High-Mobility n-Type Charge-Carriers in Large Single-Crystals of Anatase (TiO_2). *J. Appl. Phys.* **1994,** 75, 633-635.
8. Hölzl, J.; Schulte, F., Work Function of Metals. In *Solid Surface Physics*, Springer: 1979; pp 1-150.
9. Riviere, J. C., Work Function: Measurement and Results. In *Solid State Surface Science*, Green, M., Ed. Decker: New York, 1969.
10. Michaelson, H. B., The Work Function of the Elements and Its Periodicity. *J. Appl. Phys.* **1977,** 48, 4729-4733.